Isotope specific resolution recovery image reconstruction in high resolution PET imaging

Fotis A. Kotasidis
Division of Nuclear Medicine and Molecular Imaging, Geneva University Hospital, CH-1211 Geneva, Switzerland and Wolfson Molecular Imaging Centre, MAHSC, University of Manchester, M20 3LJ, Manchester, United Kingdom

Georgios I. Angelis
Faculty of Health Sciences, Brain and Mind Research Institute, University of Sydney, NSW 2006, Sydney, Australia

Jose Anton-Rodriguez and Julian C. Matthews
Wolfson Molecular Imaging Centre, MAHSC, University of Manchester, Manchester M20 3LJ, United Kingdom

Andrew J. Reader
Montreal Neurological Institute, McGill University, Montreal QC H3A 2B4, Canada and Department of Biomedical Engineering, Division of Imaging Sciences and Biomedical Engineering, King's College London, St. Thomas' Hospital, London SE1 7EH, United Kingdom

Habib Zaidi
Division of Nuclear Medicine and Molecular Imaging, Geneva University Hospital, CH-1211 Geneva, Switzerland; Geneva Neuroscience Centre, Geneva University, CH-1205 Geneva, Switzerland; and Department of Nuclear Medicine and Molecular Imaging, University of Groningen, University Medical Center Groningen, PO Box 30 001, Groningen 9700 RB, The Netherlands

Purpose: Measuring and incorporating a scanner-specific point spread function (PSF) within image reconstruction has been shown to improve spatial resolution in PET. However, due to the short half-life of clinically used isotopes, other long-lived isotopes not used in clinical practice are used to perform the PSF measurements. As such, non-optimal PSF models that do not correspond to those needed for the data to be reconstructed are used within resolution modeling (RM) image reconstruction, usually underestimating the true PSF owing to the difference in positron range. In high resolution brain and preclinical imaging, this effect is of particular importance since the PSFs become more positron range limited and isotope-specific PSFs can help maximize the performance benefit from using resolution recovery image reconstruction algorithms.
Methods: In this work, the authors used a printing technique to simultaneously measure multiple point sources on the High Resolution Research Tomograph (HRRT), and the authors demonstrated the feasibility of deriving isotope-dependent system matrices from fluorine-18 and carbon-11 point sources. Furthermore, the authors evaluated the impact of incorporating them within RM image reconstruction, using carbon-11 phantom and clinical datasets on the HRRT.
Results: The results obtained using these two isotopes illustrate that even small differences in positron range can result in different PSF maps, leading to further improvements in contrast recovery when used in image reconstruction. The difference is more pronounced in the centre of the field-of-view where the full width at half maximum (FWHM) from the positron range has a larger contribution to the overall FWHM compared to the edge where the parallax error dominates the overall FWHM.
Conclusions: Based on the proposed methodology, measured isotope-specific and spatially variant PSFs can be reliably derived and used for improved spatial resolution and variance performance in resolution recovery image reconstruction. The benefits are expected to be more substantial for more energetic positron emitting isotopes such as Oxygen-15 and Rubidium-82. © *2014 American Association of Physicists in Medicine*. [http://dx.doi.org/10.1118/1.4870985]

Key words: point spread function, positron range, radioactive printing, HRRT, PET, brain imaging

1. INTRODUCTION

Statistical image reconstruction algorithms incorporating scanner-specific PSFs enable the relationship between image and projection space to be accurately characterized and modeled within the system matrix. Such resolution recovery image reconstruction algorithms have been shown to improve both signal-to-noise ratio and spatial resolution, leading to more accurate quantification.[1] Despite the added complexity of such algorithms, their aforementioned attributes have led recently to their introduction on most commercial scanners.[2,3] Whether implemented in image or projection space, these algorithms are usually based on an accurate estimation of the spatially invariant or variant PSF.[4] Analytic calculations and

Monte Carlo simulations can be used to estimate the physics-related component of the scanner's system matrix including crystal penetration, intercrystal scattering, photon noncolinearity, and positron range in the form of a spatially varying point spread function.[5–9] However, models derived with such methods need to be validated against data taken from real measurements. Consequently, experimental evaluation of the scanner's spatially variant PSFs is the preferred method for evaluating its spatial resolution characteristics and generating accurate system matrices to be used within resolution recovery image reconstruction algorithms.[2,3,10–16] Such measurements are usually performed using a point source, to sample the PSF at different locations in the field-of-view (FOV). Since only a finite number of locations can be sampled, a parameterization of the system's response is used, with the estimated parameters further fitted to smooth functions, such as polynomials, to interpolate the parameters in the remaining not sampled positions. Due to the large number of PSF samples needed, long lived isotopes not used in clinical practice such as Gallium-68[2,12] and Sodium-22[3,4,11,17] are usually the isotopes of choice. Although the PSFs measured with these isotopes inherently incorporate positron range blurring, in some cases these isotopes have a small positron range, in which case can be ignored or the point source is encapsulated in such a way that the positron annihilations are considered to be localized within the point source casing. Either way, the PSF models derived from such measurements are considered to model only the detector related blurring.[1] However, this means that when these PSF models are incorporated within image reconstruction, they do not correspond to the actual blurring in the measured data, usually underestimating the true PSF, owing to the difference in positron range, thus leading to suboptimal resolution recovery during reconstruction. In whole body PET/CT scanners, this effect can only be of importance when the difference in positron range between the isotopes used to measure the PSF and of that used to perform the imaging study (phantom or clinical study) is substantial. This is true as the spatial resolution is dominated by scanner-specific resolution degrading effects and the PSF is less susceptible upon changes in the isotope's positron range. However, in high resolution brain or preclinical PET imaging, the PSF becomes more isotope-dependent since all the detector related resolution degrading effects account less in the overall spatial resolution and positron range becomes the limiting resolution degradation factor. Thus, over or underestimation of the true PSF is accentuated with potential benefits from using isotope-specific kernels within RM image reconstruction.[18–20]

Positron range blurring being considered as an effect acting on image space could be modeled separately from the detector blurring component.[1] Such separable positron range models have been reported in the literature using either analytic or Monte Carlo methods for both uniform[5,19–23] and heterogeneous media with varying properties.[24–30] However, these models again need experimental validation. Measuring spatially variant isotope-specific PSFs from short-lived clinically used isotopes is very challenging owing to the rapid decay and the multitude of positions that need to be sam-

pled and to best of our knowledge, experimental derivation of isotope-specific PSF maps has not been reported before. However, a previously proposed technique based on printing an array of point sources to simultaneously sample the PSF at multiple positions can facilitate measurements from short-lived isotopes (not previously practical with single source acquisitions based on robotic equipment), enabling experimental isotope specific PSFs to be derived and used within image reconstruction.[10] In our previous work, we demonstrated the feasibility of using radioactive point source printing to derive experimentally measured kernels and evaluated their application in the framework of resolution recovery image reconstruction.

In this work, we apply such a technique to demonstrate the feasibility of deriving combined isotope-specific PSF maps for two clinically used isotopes on the HRRT PET scanner. Moreover, we evaluate the effect of positron range on the spatially variant PSF. Following PSF estimation, we evaluate the clinical impact of incorporating isotope-dependant PSFs within image reconstruction[31] using a recently implemented fully 3D spatially variant resolution modeling (SVRM) reconstruction on the HRRT based on the ordinary Poisson ordered subsets expectation maximization algorithm (OPOSEM).

2. METHODS

2.A. Point source production using fluorine-18 and carbon-11

Initial measurements were performed using two isotopes, namely, fluorine-18 and carbon-11, with a half-life of ∼110 and ∼20 min, respectively. The mean positron range for carbon-11 and fluorine-18 is 1.266 and 0.660 mm, respectively, with a theoretical difference of 0.606 mm between them.[20] Radioactive printing has been used previously to measure the resolution properties of PET scanners and such a technique can provide fast, uniform, and reproducible sources of arbitrary two-dimensional activity distributions.[10,15] In this work, a printer was used to print an array of 11 × 15 (axially × radially) radioactive point sources, 1 mm in diameter with a 1.85 and 1.95 cm radial and axial sampling distance, respectively. Black ink was mixed with ∼1 GBq of fluorine-18 and/or carbon-11 solution (0.1–0.2 ml) via injection into a modified cartridge. The array was printed once for the fluorine-18 point sources while for the carbon-11 point sources it was re-printed three times to boost the activity and counteract the rapid decay and reduced counting statistics compared to fluorine-18.

2.B. Scanning protocol

Following point source printing, the array was placed horizontally in the HRRT FOV, using a custom made Perspex phantom, covering almost the entire radial (−12.95.. + 12.95 cm) and axial (−9.75... + 9.75 cm) FOV (Fig. 1). The phantom facilitated accurate and highly reproducible positioning of the array and provided tissue equivalent annihilating material for the positrons. The phantom was made out of 2 Perspex endplates held by 4 Perspex rods with axial and
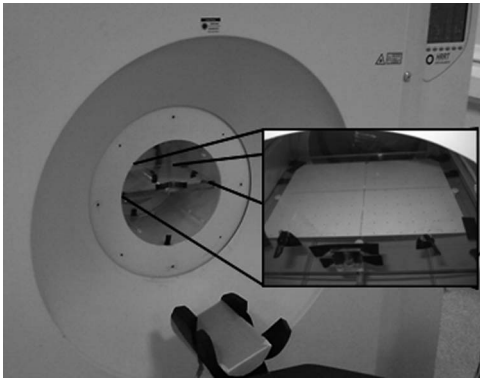
FIG. 1. The HRRT scanner was used to sample and evaluate the isotope-specific PSFs. For this purpose, a custom made Perspex phantom tightly positioned in the FOV was used to sandwich an array of printed radioactive point sources.

transverse dimensions equal to the HRRT's bore, ensuring a tight fit during positioning.[32] Data were acquired in 64-bit list mode format during two scanning sessions. In the first session, the array was scanned for 20 min using fluorine-18 ($\sim$100 million prompts), while it was scanned for $\sim$60 min in the second session using carbon-11 ($\sim$65 million prompts). Following data acquisition, a 6 min transmission scan was also acquired in both sessions for attenuation correction. The data were histogrammed and reconstructed using standard HRRT software without resolution modeling, including all corrections for erroneous events (OP-OSEM, 10 iterations - 16 subsets).[33] Images were reconstructed in a $256 \times 256 \times 207$ voxel grid, with a 1.21875 mm $\times$ 1.21875 mm $\times$ 1.21875 mm voxel size (Fig. 2).

2.C. Parameter fitting and isotope specific resolution modeling image reconstruction

Following image reconstruction, the PSFs were fitted in image space using a Gaussian mixture model of two 3D Gaussians with axial, radial, and tangential mean and standard deviation components for each Gaussian, as well as a weighting
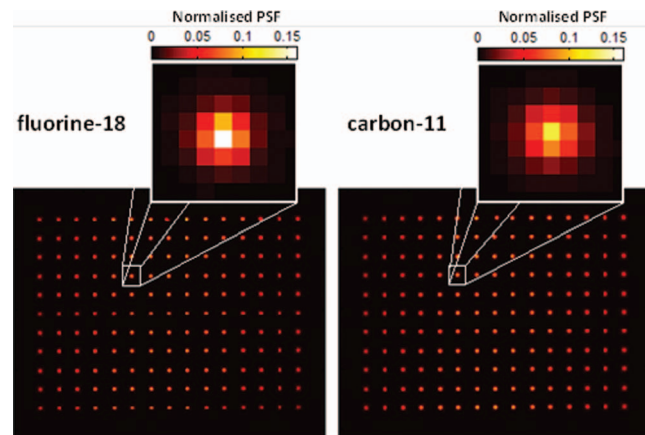

FIG. 2. Horizontal planes through the reconstructed point sources using fluorine-18 and carbon-11 along with zoomed and normalized 2D kernels. The carbon-11 kernel appears less sharp with more activity spilling in the surrounding voxels.

parameter controlling the mixing of the two distributions.[10] Specifically, each reconstructed kernel was modeled as

$$PSF(\mathbf{x}, \mathbf{x}') = \sum_{i=1}^{2} w_i G_i(\mathbf{x}, \boldsymbol{\mu}(\mathbf{x}'), \boldsymbol{\Sigma}(\mathbf{x}')), \sum_{i=1}^{2} w_i = 1,$$

(1)

$$G_i(\mathbf{x}, \boldsymbol{\mu}(\mathbf{x}'), \boldsymbol{\Sigma}(\mathbf{x}')) = \frac{1}{(2\pi)^{3/2} |\boldsymbol{\Sigma}(\mathbf{x}')|^{1/2}}$$

$$\exp\left(-\frac{1}{2}(\mathbf{x} - \boldsymbol{\mu}(\mathbf{x}'))^T \boldsymbol{\Sigma}(\mathbf{x}')^{-1}(\mathbf{x} - \boldsymbol{\mu}(\mathbf{x}'))\right),$$

(2)

$$\boldsymbol{\mu} = \begin{pmatrix} \mu_\gamma(\mathbf{x}') \\ \mu_t(\mathbf{x}') \\ \mu_\zeta(\mathbf{x}') \end{pmatrix} \boldsymbol{\Sigma} = \begin{pmatrix} \sigma_\gamma^2(\mathbf{x}') & 0 & 0 \\ 0 & \sigma_t^2(\mathbf{x}') & 0 \\ 0 & 0 & \sigma_\zeta^2(\mathbf{x}') \end{pmatrix},$$

(3)

where $\mathbf{x}$ and $\mathbf{x}'$ are position vectors concerning the image space and PSF kernel, G_i is the function describing a three-dimensional Gaussian distribution and w_i is the mixing proportion between the two Gaussian distributions. The matrices $\boldsymbol{\mu}$ and $\boldsymbol{\Sigma}$ hold the first and second order moments of the PSF (mean and covariance) for the radial, tangential, and axial (γ, t, ζ) components. The constants in front of the exponential are normalization constants, such that the integral of Eq. (2) is equal to 1. The Expectation Maximization (EM) algorithm was used to estimate the parameters using the above Gaussian mixture model (*gmdistribution* class - The Mathworks). In total, 13 parameters were estimated for each of the 165 point sources and for both the fluorine-18 and carbon-11 arrays.

To estimate the parameters in the remaining positions in the FOV, a further parameterization was used and the estimated PSF parameters at the measured positions were fitted to quadratic polynomial functions to interpolate the parameters at the unmeasured positions. Since the PSF on the HRRT is almost invariant under axial transformations, the image space 3D PSF kernels for each isotope were precalculated for a single slice and applied to all axial planes during image reconstruction.[15]

The measured isotope-specific and spatially variant kernels were incorporated in a previously developed spatially variant image-space resolution modeling image reconstruction algorithm for the HRRT.[31] The algorithm is a modified version of the standard resolution modeling OP-OSEM algorithm used on the scanner:[33]

$$\lambda_j^{(t+1)} = \frac{\lambda_j^{(t)}}{\sum_k q_{jk} s_k} \sum_k q_{jk} \sum_i \frac{p_{ik} m_i}{y_i^{(t)}}$$

(4)

with

$$s_k = \sum_i p_{ik} a_i n_i$$

(5)

and

$$y_i^{(t)} = \sum_{k'} p_{ik'} \sum_{j'} q_{j'k'} \lambda_{j'}^{(t)} + \frac{(r_i + sc_i)}{a_i n_i},$$

(6)

where $\boldsymbol{\lambda} = \{\lambda_j\} \in \mathfrak{R}^N$, $\lambda_j \geq 0$ is the unblurred image, $\mathbf{p} = \{p_{ik}\} \in \mathfrak{R}^{M \times N}$, $p_{ik} \geq 0$ is the geometric components of

the system matrix between the ith projection bin and the kth image voxel, $\mathbf{q} = \{q_{jk}\} \in \mathfrak{R}^{N \times N}$, $q_{jk} \geq 0$ is the blurring component of the system matrix between the jth and kth image voxels, $\mathbf{s} = \{s_k\} \in \mathfrak{R}^N$ is the sensitivity image, $\mathbf{m} = \{m_i\} \in \mathbb{Z}^M$, $m_i \geq 0$ is the projection data in the ith projection bin, $\mathbf{n} = \{n_i\} \in \mathfrak{R}^M$ and $\mathbf{a} = \{a_i\} \in \mathfrak{R}^M$ are the normalization and attenuation efficiencies in the ith projection bin, while $\mathbf{r} = \{r_i\} \in \mathfrak{R}^M$ and $\mathbf{sc} = \{sc_i\} \in \mathfrak{R}^M$ are the mean random and scatter events, and t is the iteration number.

2.D. Evaluation of isotope-specific system matrices

To assess the impact of using isotope-specific PSF compared to the standard PSF (being non-specific to the isotope of the study to be reconstructed), we used carbon-11 datasets. To assess the spatial resolution characteristics, we used carbon-11 point source data and a single scan of the point source array was acquired for 60 min collecting 69×10^6 prompts. To evaluate bias-variance performance, the Esser image quality phantom was scanned. The 8, 12, 16, and 25 mm diameter hot cylinders were filled with carbon-11 with a 4:1 ratio over the warm background. Two 25 mm cylinders were left empty and along with a 25 mm solid cylinder represented cold regions. Data were acquired in list-mode for 120 min collecting 8.7×10^8 prompts. Data were analyzed qualitatively as well as quantitatively. For quantification, the activity concentration from sample volumes taken from the cylinders and the background was measured in a well counter after applying all necessary corrections (decay, dead time, background, and volume corrections). Following the NEMA standards for evaluating image quality (60 ROIs /per cylinder size over the 5 planes) two figures of merit were calculated and referred to as the contrast recovery coefficient (CRC) [Eqs. (7) and (8)] and image roughness (IR) [Eq. (9)]:[34]

$$CRC_{h,j} = \frac{\left(C_{h,j}\big/C_{bg,j} - 1\right)}{\left(a_h\big/a_{bg} - 1\right)} \cdot 100\%, \tag{7}$$

$$CRC_{c,j} = \frac{C_{bg,j} - C_{c,j}}{C_{bg,j}} \cdot 100\%, \tag{8}$$

$$IR_{j,k} = \frac{\sqrt{\sum\limits_{p=1}^{P}\left(C_{bg,j,k,p} - C_{bg,j,k}\right)^2 \Big/ \left(P_{bg,j} - 1\right)}}{C_{bg,j,k}},$$

$$IR_j = \frac{\sum\limits_{k=1}^{N} IR_{j,k}}{N_{bg}}, \quad N_{bg} = 60, \tag{9}$$

where $C_{h,j}$ and $C_{c,j}$ are the mean reconstructed activity concentrations (AC) for the jth hot and cold cylinders, respectively, $C_{bg,j}$ is the mean reconstructed AC for the jth background cylinder averaged over the 60 ROIs of equal size, a_h and a_{bg} are the measured ACs in the hot cylinders and the background, $C_{bg,j,k}$ is the mean AC for the jth background cylinder size and the kth ROI, $C_{bg,j,k,p}$ is the reconstructed

AC for the pth image voxel within the kth ROI for the jth background cylinder, and $P_{bg,j}$ is the number of pixels in the jth background cylinder.

Finally, a single clinical [^{11}C]methionine dataset from a patient with a grade II oligodendroglioma was used for qualitative assessment.[35] The patient was injected on the scanner's bed with 430 MBq of [^{11}C]methionine followed by a 60 min list-mode data acquisition and a 6 min transmission scan for attenuation correction. Data acquired following the first 10 min postinjection were histogrammed into a single frame and used to evaluate the different PSF maps within the reconstruction.

All carbon-11 datasets were reconstructed using 2 SVRM reconstructions: the one using the fluorine-18 derived PSF map, representing our standard spatially variant PSF map available on the HRRT (nonisotope specific SVRM reconstruction) and the one using the carbon-11 derived PSF map, representing the isotope specific PSF map (isotope specific SVRM reconstruction). As such, the fluorine-18 based SVRM reconstruction should underestimate the true PSF on the carbon-11 datasets compared to the carbon-11 based SVRM reconstruction which should provide a better match. For comparison, the datasets were also reconstructed using OP-OSEM without RM (no RM),[33] as well as with the HRRT user's community spatially invariant RM (SIRM) reconstruction.[36]

3. RESULTS

3.A. Experimentally derived isotope-specific system matrices

The tangential, radial, and axial standard deviation obtained from the Gaussian mixture model is plotted in Fig. 3 as a function of radial distance for both the fluorine-18 and carbon-11 derived PSFs. Data for each radial position were averaged across all 11 axial point source positions in order to include more data points and reduce the variance in the estimated parameters since the image space PSF on the HRRT can be considered almost invariant under axial transformations.[15] The standard deviation is plotted both for the 1st and the 2nd Gaussian distributions used in our Gaussian mixture model. The 1st Gaussian accounts for the main fast decaying part of the PSF and, therefore, has a smaller standard deviation compared to the 2nd Gaussian, which accounts for the tails of the PSF and as such, is broader. The kernels are broader in the axial direction followed by the radial and the tangential direction, which is in accordance to previous measurements on the HRRT using the same printing technique.[15] Looking across the two isotopes, carbon-11 appears to produce kernels with slightly larger standard deviation compared to fluorine-18 with the trend being evident in both Gaussian distributions. However, the difference appears to be more pronounced toward the centre of the FOV with the standard deviation between the two isotopes being more closely matched toward the edge of the radial FOV. This effect is more easily discernible in the standard deviation from the 1st Gaussian as it appears less noisy compared to the 2nd Gaussian due to the latter being more susceptible to noise around the PSF tails. Since the PSF on the HRRT is almost
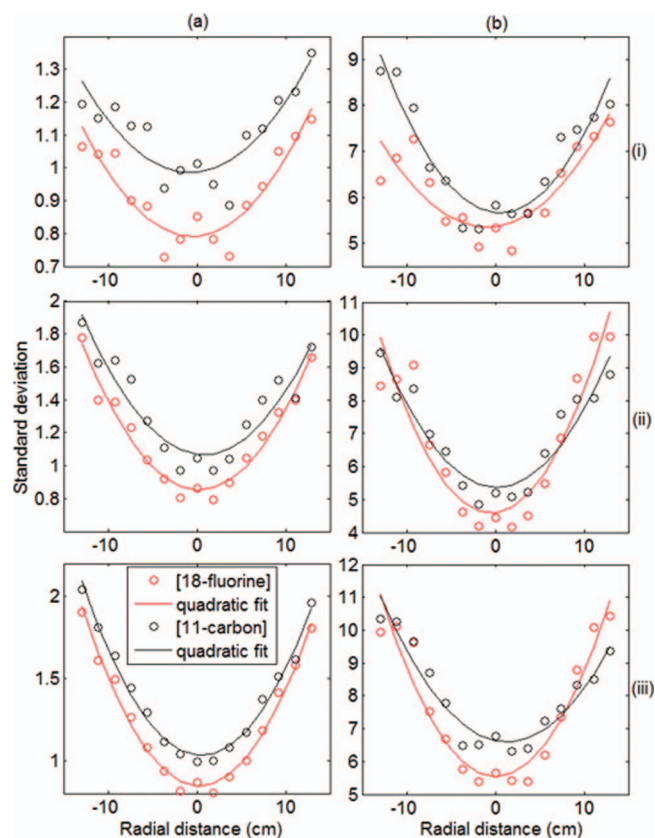
FIG. 3. Parameters further fitted to functions assuming smooth response transitions to calculate a parameterized response throughout the FOV. Graphs of tangential (i), radial (ii), and axial (iii) standard deviation versus radial distance (axially averaged) for the 1st (a) and 2nd (b) Gaussian and for both isotopes along with the corresponding quadratic fits. Similar fits were estimated for every parameter.
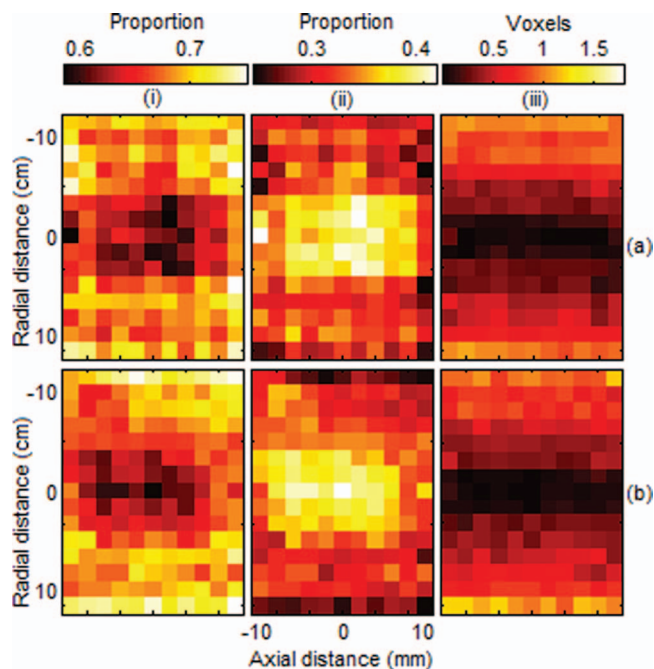

FIG. 4. Parametric maps of the proportion coefficient between the 1st (i) and 2nd (ii) Gaussian distribution (sum to 1) for Carbon-11 (a) and Fluorine-18 (b) as well as the respective radial asymmetry for each isotope given as the displacement between the radial means of the two Gaussian distributions in voxel units (iii).

invariant under axial and rotational transformations, parameter interpolation was used only radially, to describe its variation as a function of radial distance.[15] Having two Gaussian distributions to model the PSFs, each modeling a different component of the PSF, the difference between the two isotopes with respect to the percentage contribution of each Gaussian is of interest. Indeed changes to the Gaussian percentage contribution between different isotopes could provide insights into the effect of positron range on the shape of the scanner's overall PSF, especially since the PSF attributed to positron range is not exactly Gaussian but has a "cusp like" shape.[19] Parametric maps of the mixing proportions between the two Gaussians are shown in Fig. 4, both for carbon-11 and fluorine-18. Furthermore, Fig. 4(iii) shows the radial asymmetry given as the difference in the radial means between the two Gaussians for the two isotopes. The percentage proportion of the 2nd Gaussian is high in the centre of the radial FOV, while the 1st Gaussian accounts for a larger percentage of the PSF toward the edge of the radial FOV.

However, no apparent difference is seen between the two isotopes potentially signifying that going from fluorine-18 [Fig. 4(b)] to carbon-11 [Fig. 4(a)], the increase in the standard deviation, especially toward the centre of the FOV, can be equally attributed to an increase in the central fast decreasing part of the distribution accounted for by the 1st Gaussian and

the slowly decreasing tails accounted for by the 2nd Gaussian. Similarly, looking at the radial asymmetry and comparing it across the two isotopes, no apparent difference is seen, with the PSFs being equally asymmetric moving progressively toward the edge of the FOV and with a maximum displacement of ~1.3 voxels (~1.6 mm) between the two distributions. This agrees well with the theory since the asymmetry is caused by the parallax error and, as such, it should be independent of the positron range.

Parametric maps of the FWHM are shown in Fig. 5 for fluorine-18 [Fig. 5(i)] and carbon-11 [Fig. 5(ii)] PSFs. For both isotopes, the axial FWHM is the highest, followed by the radial and tangential. A comparison between the two isotopes shows consistently higher FWHM values for carbon-11 in all directions with the axial FWHM increasing by ~14% (2.59–2.91 mm) at the centre of the radial FOV (z = 0, r = 0) and by ~3.7% (3.78–3.92 mm) at the edge of the radial FOV (z = 0, r = 12.9 cm). Similar variations are observed in the radial and tangential FWHM. The difference in FWHM between the two isotopes is visualized as a parametric image in Fig. 5 (iii). The quantitative difference in the FWHM between the two isotopes can be summarized in Fig. 6. The axial, radial, and tangential FWHM is plotted as a function of the radial distance for the two isotopes with the box representing the FWHM axial deviation at each radial position and the whiskers showing the 25th and 75th percentile. What is immediately apparent is that the FWHM difference is more pronounced in the centre of the radial FOV (also seen in Fig. 3) with differences up to ~0.38 mm in the axial, radial, and tangential FWHM, while at the edge of the radial FOV the differences are less distinct (up to ~0.2 mm).
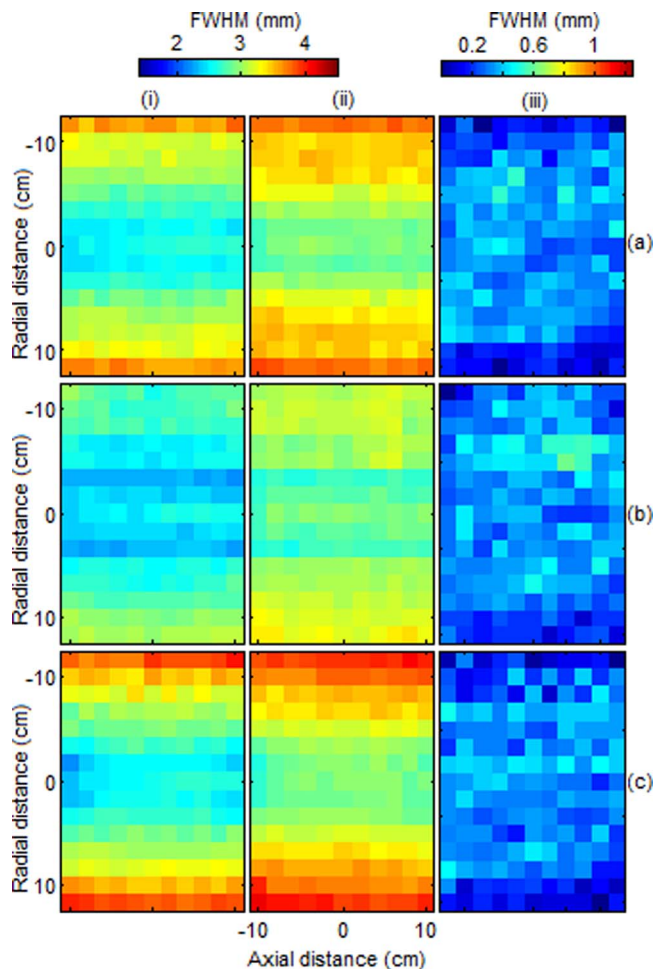
FIG. 5. Parametric maps of radial (a), tangential (b), and axial (c) FWHM on the HRRT as a function of radial and axial distance for Fluorine-18(i), Carbon-11(ii), and their difference (iii).

These results are in agreement with Fig. 3 and can be explained by the small detector blurring effect that manifests in a large contribution of positron range on the overall PSF in the centre of the FOV as opposed to the edges where the parallax effect is clearly the dominating resolution degrading factor.

3.B. Evaluation of isotope-specific system matrices within resolution recovery image reconstruction

The parameterized isotope-specific kernel maps were incorporated within the aforementioned spatially variant image reconstruction algorithm using a factorized system matrix as presented in Ref. 31. Evaluation was performed using carbon-11 point source, phantom, as well as clinical datasets acquired on the HRRT.

Figure 7 shows graphs of contrast recovery (CR) versus image roughness (IR) for the 25 mm hot (i) and cold (ii) cylinders in the Esser phantom, for up to 20 OSEM iterations (16 subsets) using the four different reconstruction algorithms introduced at the end of Sec. 2.D. In the cold cylinder, the carbon-11 SVRM reconstruction has a ~94% CR compared to ~92% for the fluorine-18 SVRM, ~88% for the SIRM
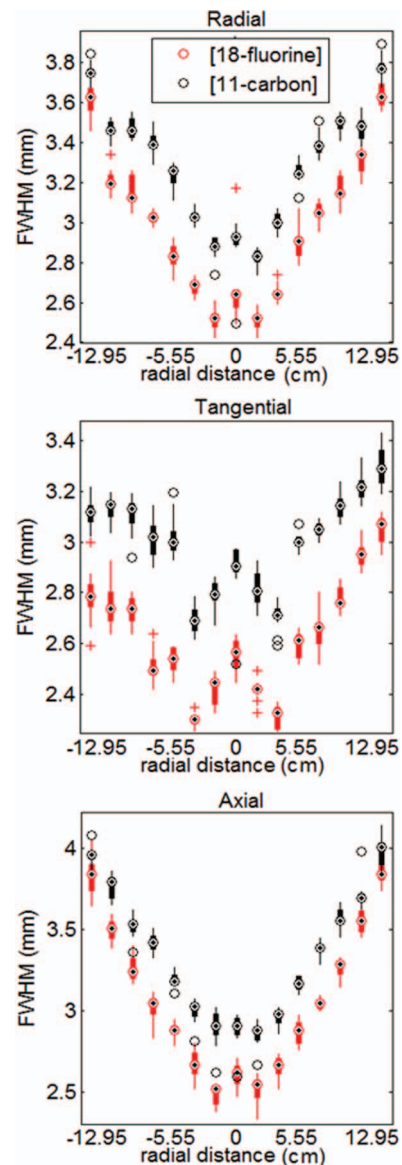

FIG. 6. Box-Whisker plots of the radial, tangential, and axial FWHM versus radial distance for Carbon-11 and Fluorine-18, where each box represents the axial variation of the FWHM with the top and bottom showing the 25th and 75th percentile.

reconstruction, and ~75% for the no RM reconstruction, at the same variance level. In the hot cylinder, both SVRM reconstruction methods outperform the standard SIRM and no RM reconstructions; however, no substantial difference can be seen between the 2 SVRM reconstructions even after 20 iterations. Although the carbon-11 SVRM method should provide a better resolution modeling due to the PSF kernel being more representative of data blurring caused by positron range, it appears to converge slower compared to fluorine-18 SVRM. Both follow the same bias-variance path with the slower convergence on the carbon-11 SRVM probably attributed to the broader PSF kernel with longer tails and potentially more than 20 iterations are needed to see any bias-variance performance improvement. Based on the bias-variance graphs, images from a plane traversing the seven hot and cold cylinders are shown in Fig. 8 for all the
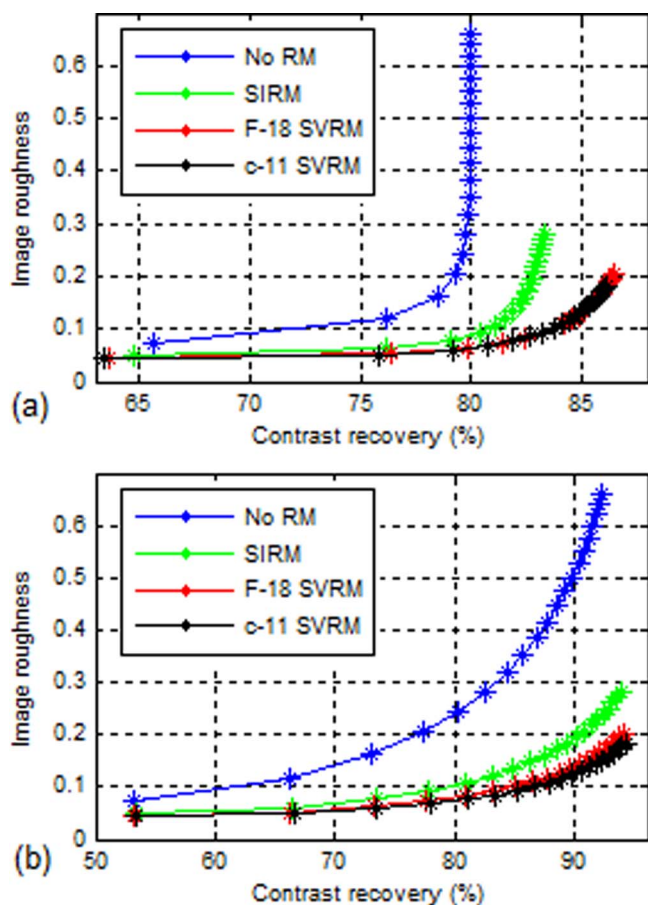
FIG. 7. Percentage contrast recovery (CR) versus image roughness (IR) for the 25 mm (a) hot and (b) cold cylinders from the carbon-11-filled Esser image quality phantom using the four different algorithms.
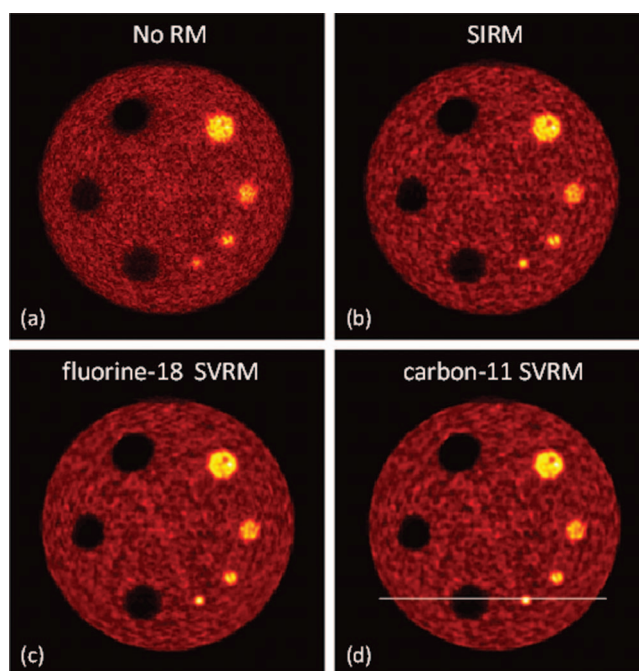
FIG. 8. Reconstructed images of the carbon-11 filled Esser image quality phantom at matched variance level using (a) no RM (4 iter), (b) HRRT user's SIRM (12 iter), (c) fluorine-18 SVRM (16 iter), and (d) the carbon-11 SVRM (20 iter) reconstruction.

reconstructions and at matched variance level (20th iteration for the carbon-11 SVRM, 16th iteration for the fluorine-18 SVRM, 12th iteration for the SIRM, and 4th iteration for the no RM reconstructions). The contrast improvements offered by the SVRM reconstructions are evident, however, no substantial qualitative difference is observed between the carbon-11 and fluorine-18 SVRM reconstructions. Nevertheless, the carbon-11 SVRM offers slightly improved contrast especially in the small 8 mm cylinder, as can be seen from the profile plot in Fig. 9 and slightly better resolution recovery at the boundaries. Gibbs artifacts appear in the phantom boundaries in both SVRM reconstructions shown in Fig. 8; however, these are not very pronounced. Furthermore, despite the kernel used in the carbon-11 SVRM reconstruction being wider compared to the one used in the fluorine-18 SVRM it does not appear to enhance them. Furthermore, no Gibbs artifacts are clearly visible in the boundaries of the hot cylinders.

The impact of the measured isotope specific kernels on resolution recovery is depicted in Fig. 10 where one-dimensional profiles from the carbon-11 point sources are plotted at progressively increasing radial distance (20th iteration). Resolution recovery is more pronounced using the carbon-11 SVRM reconstruction despite its slower convergence compared to the fluorine-18 SVRM reconstruction, seen in the

bias-variance graphs from Fig. 7. However, at the 20th iteration all reconstructions have almost converged (after 15th iteration no substantial change was seen, as point sources is air converge relatively fast compared to hot cylinders in warm background) showing the improved resolution characteristics obtained by using the isotope specific PSF within the reconstruction.

Finally reconstructed images of the clinical [^{11}C]methionine dataset are shown in Fig. 11 for all methods, as well as the difference between the isotope specific and non-specific SVRM reconstructions (carbon-11 - fluorine-18). Data are shown again at similar variance level using the same iterations for each reconstruction method, as in Fig. 8. Slightly increased contrast is obtained in the carbon-11 SVRM reconstruction looking at the difference image, with the improvements located at the boundaries of regions with high activity
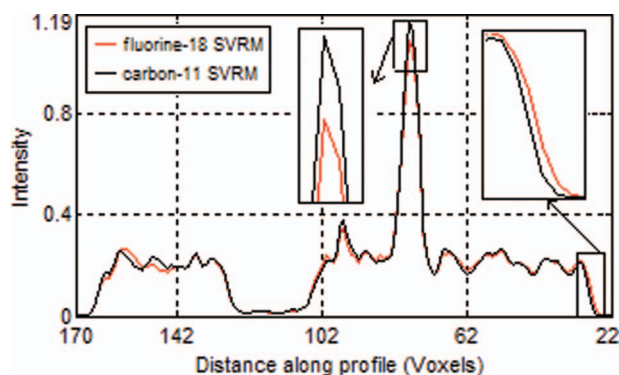

FIG. 9. 1-D profile through the reconstructed fluorine-18 SVRM (16 iter), and carbon-11 SVRM (20 iter) reconstructions [Fig. 8 (c) and (d)].
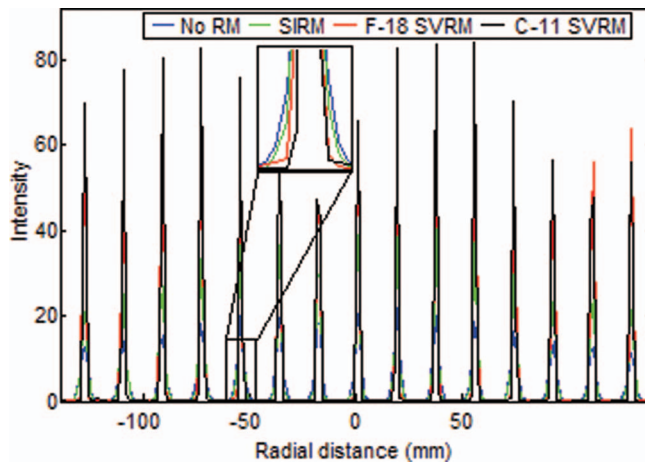
FIG. 10. 1D profile through the reconstructed carbon-11 point sources using all four reconstruction methods. Using the carbon-11 SVRM methods improved resolution recovery is obtained looking at the tails of the zoomed PSF.

gradient and with a peak uptake difference in the tumor of 1%–1.5%. Increased contrast is also seen in the pituitary gland where the lack of blood-brain barrier and the hormones produced by it result in increased uptake of amino acid based tracers such as [^{11}C]methionine.

4. DISCUSSION

From the results presented using a high resolution scanner, such as the HRRT, where all the detector related resolution degradation effects contribute less to the overall spatial resolution compared to a whole body scanner, even the small difference in positron range between fluorine-18 and carbon-11 is sufficient to affect the overall PSF. This effect is less distinct toward the edge of the radial FOV and can be attributed to the fact that parallax error has a significantly larger contribution to the FWHM compared to the centre of the FOV and any increase in the positron range will have a smaller

impact on the overall FWHM. In the centre of the radial FOV differences of up to 0.38 mm FWHM were found between the two isotope PSF maps, with smaller differences in the FWHM at the edge of the FOV. Comparing these experimental values with the theoretical increase on the overall FWHM, going from fluorine-18 to carbon-11, generally a good agreement is obtained. Considering the empirical formula of Derenzo and Moses,[37,38] the FWHM of the overall PSF can be described as

$$\mathrm{fwhm}_{\mathrm{overall}} = k\sqrt{\mathrm{fwhm}_{\mathrm{positron}}^2 + \mathrm{fwhm}_{\mathrm{other}}^2} \qquad (10)$$

where k is a parameter between $1.1 < k < 1.3$ depending on the reconstruction algorithm and other effects apart from positron range include noncolinearity, crystal size, parallax effects, and position decoding accuracy. However, due to the cusp-like shape of the positron range PSF, using the effective FWHM given as 2.35 rms is a more meaningful measure of the blurring caused by the positron range distribution, as the positron range density function is very peaked and indices depending on the peak height, such as FWHM, are not meaningful.[19,20] Taking into account a theoretical rms value (in water) of 0.2 for fluorine-18 as reported by Derenzo,[39] ($k = 1.1$) with a fluorine-18 based $\mathrm{fwhm}_{\mathrm{overall}}$ of 2.6 mm (see Fig. 5) at the centre of the FOV, the $\mathrm{fwhm}_{\mathrm{other}}$ is estimated to be ∼2.3 mm. Using the estimated $\mathrm{fwhm}_{\mathrm{other}}$ of 2.3 mm then and a theoretical rms value for carbon-11 of 0.39 mm,[39] the $\mathrm{fwhm}_{\mathrm{overall}}$ should increase by ∼0.12 mm, which is lower than the maximum reported difference of 0.38 mm in Fig. 5. However, using rms values reported by Fiedler *et al.*[23] with 0.327 mm and 0.594 mm rms for fluorine-18 and carbon-11, respectively, the theoretical increase in the $\mathrm{fwhm}_{\mathrm{overall}}$ is estimated ∼0.29 mm which provided a closer estimate to the experimental difference in the FWHM between the two isotopes.

It was observed that when using carbon-11, the increase in the FWHM compared to fluorine-18 was variable, with the spatial resolution degrading less toward the edge of the radial FOV compared to the centre. Thus, it becomes evident that
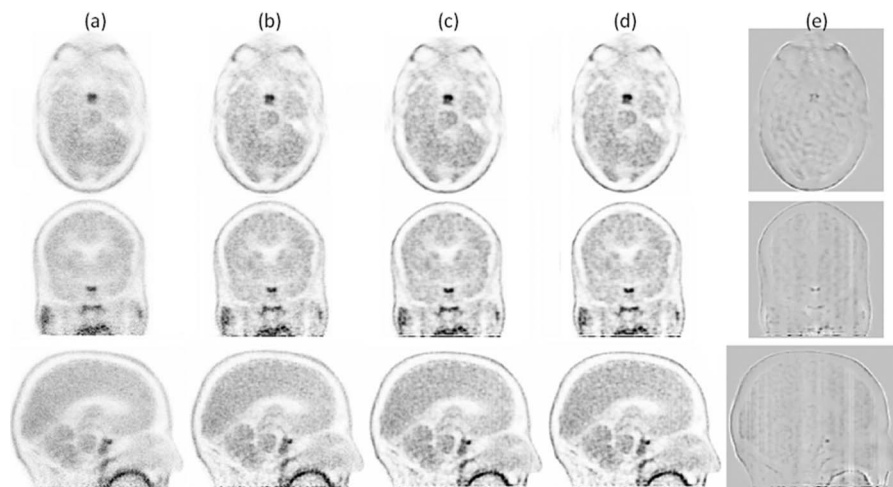

FIG. 11. Clinical study of a patient scanned on the HRRT after being injected with 430 MBq of [^{11}C]methionine reconstructed with (a) no RM (4 iter), (b) HRRT user's SIRM (12 iter), (c) Fluorine-18 SVRM (using the standard nonisotope specific PSF map) (16 iter), and (d) the Carbon-11 SVRM (using the isotope specific PSF map) (20 iter) at matched variance level, while (e) is the difference image between (d) and (c).

as the positron range becomes more significant (being spatially invariant within the scanner), the impact of the spatially variant parallax error on the FWHM is reduced, leading to a less variant PSF maps. Using isotopes with even higher positron range such as Rubidium-82, Gallium-68, or Oxygen-15, will result in the overall FWHM to be dominated by the positron range FWHM, effectively making the spatial resolution invariant throughout the FOV as the parallax error will have a small contribution in the overall resolution. As such, going to isotopes with higher positron range, even a spatially invariant PSF might be sufficient to capture the resolution degrading physics effects. Although such an effect could be seen in high resolution brain and preclinical imaging, and is less likely to occur in whole body imaging, as the detector related blurring effects and more specifically the parallax error dominate the resolution characteristics of the scanner.

In this study, we used two relatively short-lived isotopes to successfully measure isotope specific PSF maps. However, even with using a printing technique to sample simultaneously multiple points in the FOV, it becomes challenging to derive experimental isotope-specific PSF maps from more energetic faster decaying isotopes. Thus, it is expected that scanning Oxygen-15 or Rubidium-82 PSF maps can be quite challenging. Optimization of the printing and positioning protocols though could make such a scan feasible. A different approach would be to use a hybrid model to derive isotope-specific kernels from more energetic and faster decaying isotopes. Following experimental measurement of the spatially variant PSF using fluorine-18 or any other long-live isotope, the isotope's theoretical positron range distribution could be deconvolved from the overall PSF, leaving an experimental PSF including all the remaining resolution degrading effects.[39,40] Subsequently, isotope-specific PSF maps could be obtained by convolving the theoretical positron range distribution of the isotope of interest. Such an approach, although feasible, could potentially generate noisy PSF maps due to the noise amplification during the deconvolution process. However, as parameters are further interpolated using quadratic functions, noise amplification could be less of a concern.

The proposed methodology of experimentally estimating and incorporating the isotope-specific blurring within a unified measured kernel is based on the fact that it considers the positron range distribution within a uniform tissue equivalent medium. This approach constitutes a simplification due to the fact that positron range within the body is heterogeneous, depending upon the material properties the positrons traverse. A limited number of simulation and analytical based approaches have been previously reported trying to model this material dependent positron range blurring, with varying levels of improvements compared to a uniform positron range blurring as mentioned in Sec. 1. However, further evaluation is probably needed to demonstrate the potential improvements of these approaches against a uniform positron range model and justify the added complexity in their implementation.

Apart from investigating the feasibility of deriving measured isotope specific PSFs, we also evaluated their impact within isotope-specific resolution recovery image reconstruction. From the analysis performed on the Esser phantom, it was found that improvements are more noticeable in small structures and sharp edges. However, from the bias-variance graphs it was seen that in the hot cylinder and up to 20 iterations, similar bias variance performance was observed using the fluorine-18 and carbon-11 SVRM, with the carbon-11 SVRM reconstruction converging slower probably due to the slightly broader carbon-11 kernels. This is to be expected though, given the small differences between the 2 PSF maps, but also due to the fact that the bias-variance graphs in Fig. 7 correspond to the largest 25 mm cylinder (as only for this size both a cold and a hot cylinder are available in the phantom) where the small difference between the 2 isotope specific PSF maps will have a smaller impact on the bias-variance tradeoff. It is possible that after 20 iterations, the carbon-11 SVRM reconstruction providing a better match to the blurring in the carbon-11-filled Esser phantom, could outperform the fluorine-18 based reconstruction even in the largest of the cylinders. In clinical practice though even 20 iterations are considered to be excessive and time consuming and, as such, any improvements in bias-variance are going to be more subtle in larger hot regions with benefits mainly in small hot spot. A better differentiation was observed between the 2 PSF maps in cold regions with improvements visible even after 10 iterations. Improvements in both cold and hot regions might have been more notable if the cylinders were also closer to the centre of the FOV (cylinders are ~7 cm from the centre of the phantom and FOV, given the scanner and phantom z axis almost coincide) where the positron range is more influential on the measured PSF maps and improvements using the carbon-11 as opposed to the fluorine-18 PSF are expected to be slightly more pronounced. Again for more energetic positron emitting isotopes where the positron range becomes more substantial, the impact in bias-variance from using isotope-specific SVRM reconstruction as opposed to non-isotope specific SVRM reconstruction is expected to be greater. It is also expected that improvements can be obtained at less iterations despite the possibly slower convergence rate. Furthermore, the higher the positron range of the isotope used, the further away from the centre of the FOV improvements are going to be noticeable using an isotope specific resolution recovery reconstruction.

Differences of up to ~1.5% were observed on the clinical [^{11}C]methionine dataset. However, such difference between the two PSF maps is likely to vary between patients depending on the tumor size and its location in the FOV and be more pronounced for smaller tumors centrally localized in the scanned FOV. With the standard analysis on the [^{11}C]methionine uptake data for evaluation of tumor infiltration to depend upon the ratio of peak uptake to contralateral reference region uptake, a change in the peak uptake is important.[35] Indeed, even a small change can potentially impact tumor grading for diagnosis and treatment planning. Thus, even the marginal difference between the two PSF maps used in this study could be of importance with more significant benefits to be gained for tracers based on rubidium-82 or oxygen-15 used mainly in perfusion studies.

5. CONCLUSION

Experimentally measured PSF maps are now used on most modern PET scanners with such information incorporated within resolution recovery image reconstruction algorithms. Previous methods for deriving such PSF maps using single source acquisitions necessitated the use of long-lived positron-emitting isotopes different from those used in clinical practice. Consequently, the true PSF model is over or underestimated since the overall PSF incorporates the positron range blurring of the isotope used to sample the PSF. Using such PSF models within statistical image reconstruction leads to suboptimal resolution recovery. As such, deriving isotope-specific PSF, especially in high resolution brain and preclinical imaging where the spatial resolution becomes positron range limited, could help realize the full benefit of resolution recovery image reconstruction algorithms. Using the HRRT scanner and a printing technique for simultaneous production of multiple point sources, we demonstrated the feasibility of deriving measured detector and positron blurring models from clinically used isotopes in a unified PSF map. Furthermore, using carbon-11 datasets, we demonstrated slight improvements in resolution recovery and bias-variance performance using an isotope specific resolution recovery reconstruction compared to the standard nonisotope specific resolution recovery reconstruction despite the relatively small positron range difference between fluorine-18 and carbon-11. Using more energetic positron emitting isotopes, performance improvements are expected to be more substantial given the substantial increase in positron range for isotope such as oxygen-15 and rubidium-82. However, going to more energetic isotope, which tend to decay faster, additional challenges arise requiring further optimization of the current methodology.

ACKNOWLEDGMENTS

[1] A. Rahmim, J. Qi, and V. Sossi, "Resolution modeling in PET imaging: Theory, practice, benefits, and pitfalls," Med. Phys. **40**, 064301 (15pp.) (2013).

[2] V. Y. Panin, F. Kehren, C. Michel, and M. Casey, "Fully 3D PET reconstruction with system matrix derived from point source measurements," IEEE Trans. Med. Imaging **25**, 907–921 (2006).

[3] E. Rapisarda, V. Bettinardi, K. Thielemans, and M. C. Gilardi, "Image-based point spread function implementation in a fully 3D OSEM reconstruction algorithm for PET," Phys. Med. Biol. **55**, 4131–4151 (2010).

[4] C. Cloquet, F. C. Sureau, M. Defrise, G. Van Simaeys, N. Trotta, and S. Goldman, "Non-Gaussian space-variant resolution modelling for list-mode reconstruction," Phys. Med. Biol. **55**, 5045–5066 (2010).

[5] A. Rahmim, J. Tang, M. A. Lodge, S. Lashkari, M. R. Ay, R. Lautamaki, B. M. Tsui, and F. M. Bengel, "Analytic system matrix resolution modeling in PET: An application to Rb-82 cardiac imaging," Phys. Med. Biol. **53**, 5947–5965 (2008).

[6] J. E. Ortuno, P. Guerra-Gutierrez, J. L. Rubio, G. Kontaxakis, and A. Santos, "3D-OSEM iterative image reconstruction for high-resolution PET using precalculated system matrix," Nucl. Instrum. Methods, Phys. Res. A **569**, 440–444 (2006).

[7] A. M. Alessio, P. E. Kinahan, and T. K. Lewellen, "Modeling and incorporation of system response functions in 3D whole body PET," IEEE Trans. Med. Imaging **25**, 828–837 (2006).

[8] S. Moehrs, M. Defrise, N. Belcari, A. Del Guerra, A. Bartoli, S. Fabbri, and G. Zanetti, "Multi-ray-based system matrix generation for 3D PET reconstruction," Phys. Med. Biol. **53**, 6925–6945 (2008).

[9] J. Qi, R. M. Leahy, S. R. Cherry, A. Chatziioannou, and T. H. Farquhar, "High-resolution 3D Bayesian image reconstruction using the microPET small-animal scanner," Phys. Med. Biol. **43**, 1001–1013 (1998).

[10] F. A. Kotasidis, J. C. Matthews, G. I. Angelis, P. J. Noonan, A. Jackson, P. Price, W. R. Lionheart, and A. J. Reader, "Single scan parameterization of space-variant point spread functions in image space via a printed array: The impact for two PET/CT scanners," Phys. Med. Biol. **56**, 2917–2942 (2011).

[11] A. M. Alessio, C. W. Stearns, S. Tong, S. G. Ross, S. Kohlmyer, A. Ganin, and P. E. Kinahan, "Application and evaluation of a measured spatially variant system model for PET image reconstruction," IEEE Trans. Med. Imaging **29**, 938–949 (2010).

[12] D. Wiant, J. A. Gersh, M. Bennett, and J. D. Bourland, "Evaluation of the spatial dependence of the point spread function in 2D PET image reconstruction using LOR-OSEM," Med. Phys. **37**, 1169–1182 (2010).

[13] C. C. Watson, L. Eriksson, and A. Kolb, "Physics and applications of positron beams in an integrated PET/MR," Phys. Med. Biol. **58**, L1–12 (2013).

[14] J. Zhou and J. Qi, "Fast and efficient fully 3D PET image reconstruction using sparse system matrix factorization with GPU acceleration," Phys. Med. Biol. **56**, 6739–6757 (2011).

[15] F. A. Kotasidis, G. I. Angelis, J. Henderson, A. Buckley, P. J. Markiewicz, M. Green, J. Anton-Rodriguez, W. R. Lionheart, A. J. Reader, and J. C. Matthews, "Evaluation of image based spatially variant and count rate dependant point spread functions on the HRRT PET scanner," IEEE Nucl. Sci. Symp. Conf. Rec (2011), pp. 3595–3596.

[16] F. A. Kotasidis, G. I. Angelis, J. Anton-Rodriguez, J. C. Matthews, A. J. Reader, M. Green, and H. Zaidi, "Isotope dependent system matrices for high resolution PET imaging," IEEE Nucl. Sci. Symp. Conf. Rec (2012), pp. 2925–2928.

[17] M. S. Tohme and J. Qi, "Iterative image reconstruction for positron emission tomography based on a detector response function estimated from point source measurements," Phys. Med. Biol. **54**, 3709–3725 (2009).

[18] R. Lecomte, "Technology challenges in small animal PET imaging," Nucl. Instrum. Methods, Phys. Res. A **527**, 157–165 (2004).

[19] C. S. Levin and E. J. Hoffman, "Calculation of positron range and its effect on the fundamental limit of positron emission tomography system spatial resolution," Phys. Med. Biol. **44**, 781–799 (1999); **745**, 559 (2000) (corrigendum).

[20] L. Jodal, C. Le Loirec, and C. Champion, "Positron range in PET imaging: An alternative approach for assessing and correcting the blurring," Phys. Med. Biol. **57**, 3931–3943 (2012).

[21] A. Ruangma, B. Bai, J. S. Lewis, X. Sun, M. J. Welch, R. Leahy, and R. Laforest, "Three-dimensional maximum a posteriori (MAP) imaging with radiopharmaceuticals labeled with three Cu radionuclides," Nucl. Med. Biol. **33**, 217–226 (2006).

[22] M. R. Palmer and G. L. Brownell, "Annihilation density distribution calculations for medically important positron emitters," IEEE Trans. Med. Imaging **11**, 373–378 (1992).

[23] K. Fiedler, T. Frach, W. Rutten, T. Solf, and A. Thon, "Assessment of the spatial resolution of PET scanners using a Geant4-based Monte Carlo tool," IEEE Nucl. Sci. Symp. Conf. Rec. **4**, 2549–2553 (2003).

[24] W. Lehnert, M. C. Gregoire, A. Reilhac, and S. R. Meikle, "Performance of an analytical positron range modelling approach in the context of whole body small animal and clinical PET," IEEE Nucl. Sci. Symp. Conf. Rec (2011), pp. 4285–4288.

[25] B. Bing, A. Ruangma, R. Laforest, Y. C. Tai, and R. M. Leahy, "Positron range modeling for statistical PET image reconstruction," IEEE Nucl. Sci. Symp. Conf. Rec. **4**, 2501–2505 (2003).

[26] B. Bing, R. Laforest, A. M. Smith, and R. M. Leahy, "Evaluation of MAP image reconstruction with positron range modeling for 3D PET," IEEE Nucl. Sci. Symp. Conf. Rec. **5**, 2686–2689 (2005).

[27] L. Fu and J. Qi, "A novel iterative image reconstruction method for high-resolution PET Imaging with a Monte Carlo based positron range model," IEEE Nucl. Sci. Symp. Conf. Rec. **1**, 3609–3612 (2008).

[28] A. Alessio and L. MacDonald, "Spatially variant positron range modeling derived from CT for PET image reconstruction," IEEE Nucl. Sci. Symp. Conf. Rec. **1**, 3637–3640 (2008).

[29] W. Yubin, X. Qingguo, H. Chanjuan, W. Shuyun, Z. Jin, and Y. Wang, "Probability based positron range modeling in inhomogeneous medium for PET," IEEE Nucl. Sci. Symp. Conf. Rec. **6**, 3372–3375 (2006).

[30] R. Kraus, G. Delso, and S. I. Ziegler, "Simulation study of tissue-specific positron range correction for the new biograph mMR whole-body PET/MR system," IEEE Trans. Nucl. Sci. **59**, 1900–1909 (2012).

[31] G. I. Angelis, F. A. Kotasidis, J. C. Matthews, P. J. Markiewicz, W. R. Lionheart, and A. J. Reader, "Full field spatially-variant image-based resolution modelling reconstruction for the HRRT," IEEE Nucl. Sci. Symp. Conf. Rec **1** (2012), pp. 3434–3438.

[32] P. J. Markiewicz, G. I. Angelis, F. Kotasidis, M. Green, W. R. Lionheart, A. J. Reader, and J. C. Matthews, "A custom-built PET phantom design for quantitative imaging of printed distributions," Phys. Med. Biol. **56**, N247–N261 (2011).

[33] I. K. Hong, S. T. Chung, H. K. Kim, Y. B. Kim, Y. D. Son, and Z. H. Cho, "Ultra fast symmetry and SIMD-based Projection-Backprojection (SSP) algorithm for 3-D PET image reconstruction," IEEE Trans. Med. Imaging **26**, 789–803 (2007).

[34] M. E. Daube-Witherspoon, J. S. Karp, M. E. Casey, F. P. DiFilippo, H. Hines, G. Muehllehner, V. Simcic, C. W. Stearns, L. E. Adam, S. Kohlmyer, and V. Sossi, "PET performance measurements using the NEMA NU 2-2001 standard," J. Nucl. Med. **43**, 1398–1409 (2002).

[35] D. J. Coope, J. Cizek, C. Eggers, S. Vollmar, W. D. Heiss, and K. Herholz, "Evaluation of primary brain tumors using 11C-methionine PET with reference to a normal methionine uptake map," J. Nucl. Med. **48**, 1971–1980 (2007).

[36] F. C. Sureau, A. J. Reader, C. Comtat, C. Leroy, M.-J. Ribeiro, I. Buvat, and R. Trebossen, "Impact of image-space resolution modeling for studies with the High-Resolution Research Tomograph," J. Nucl. Med. **49**, 1000–1008 (2008).

[37] S. E. Derenzo and T. F. Budinger, "Resolution limit for positron-imaging devices," J. Nucl. Med. **18**, 491–492 (1977).

[38] W. W. Moses, "Fundamental limits of spatial resolution in PET," Nucl. Instrum. Methods, Phys. Res. A **648**(Suppl. 1), S236–S240 (2011).

[39] S. E. Derenzo, "Mathematical removal of positron range blurring in high resolution tomography," IEEE Trans. Nucl. Sci. **33**, 565–569 (1986).

[40] S. F. Haber, S. E. Derenzo, and D. Uber, "Application of mathematical removal of positron range blurring in positron emission tomography," IEEE Trans. Nucl. Sci. **37**, 1293–1299 (1990).